Effects of strain and quantum confinement in optically pumped nuclear magnetic resonance in GaAs: Interpretation guided by spin-dependent band structure calculations

R. M. Wood,[1] D. Saha,[2] L. A. McCarthy,[1] J. T. Tokarski III,[1] G. D. Sanders,[2] P. L. Kuhns,[3] S. A. McGill,[3] A. P. Reyes,[3] J. L. Reno,[4] C. J. Stanton,[2,*] and C. R. Bowers[1,2,†]

[1]*Department of Chemistry, University of Florida, Gainesville, Florida 32611, USA*
[2]*Department of Physics, University of Florida, Gainesville, Florida 32611, USA*
[3]*National High Magnetic Field Laboratory, Tallahassee, Florida 32360, USA*
[4]*Sandia National Laboratories, Albuquerque, New Mexico 87185, USA*

(Received 17 September 2014; published 29 October 2014)

A combined experimental-theoretical study of optically pumped nuclear magnetic resonance (OPNMR) has been performed in a GaAs/$Al_{0.1}Ga_{0.9}As$ quantum well film epoxy bonded to a Si substrate with thermally induced biaxial strain. The photon energy dependence of the Ga OPNMR signal was recorded at magnetic fields of 4.9 and 9.4 T at a temperature of 4.8–5.4 K. The data were compared to the nuclear spin polarization calculated from the electronic structure and differential absorption to spin-up and spin-down states of the electron conduction band using a modified $\mathbf{k}\cdot\mathbf{p}$ model based on the Pidgeon-Brown model. Comparison of theory with experiment facilitated the assignment of features in the OPNMR energy dependence to specific interband Landau level transitions. The results provide insight into how effects of strain and quantum confinement are manifested in optical nuclear polarization in semiconductors.

DOI: 10.1103/PhysRevB.90.155317 PACS number(s): 71.70.Fk, 71.70.Di, 71.20.Nr, 76.70.−r

I. INTRODUCTION

The effects of quantum confinement, magnetic field, and strain on the electronic band structure of III-V semiconductors have been well studied over the years and are often exploited in device engineering to achieve enhanced or modified operating characteristics [1–9]. Incorporation of these effects into spin-dependent band structure calculations could enable rational design of spintronic devices. Comparison of experimentally measured observables to calculations is critical to the development of advanced theoretical models. Optically pumped nuclear magnetic resonance (OPNMR) probes the spin-dependent band structure because of its sensitivity to the conduction electron spin polarization generated by interband optical absorption.

Here we present an OPNMR study of a 30-nm-wide, n-doped, $Al_{0.1}Ga_{0.9}As$/GaAs quantum well (QW) array at high magnetic fields. Optical absorption to spin-up and spin-down conduction electron states is calculated for this structure based on the electronic Landau level structure calculated from a $\mathbf{k}\cdot\mathbf{p}$ model based on a modified Pidgeon-Brown (PB) model [10]. The laser photon energy ($h\nu_l$) dependence of the OPNMR signal for circularly polarized light is compared to theoretical calculations, facilitating assignment of prominent features in the experimental data to specific interband Landau level (LL) transitions.

II. BACKGROUND

In the optical nuclear polarization (ONP) effect in GaAs, hyperpolarization of lattice nuclei occurs through spin angular momentum exchange between optically pumped conduction electrons and lattice nuclei. The spin angular momentum exchange is mediated by the Fermi-contact interaction $A\,\hat{\mathbf{I}}\cdot\hat{\mathbf{S}}$, where $\hat{\mathbf{I}}$ and $\hat{\mathbf{S}}$ are the nuclear and electron spin angular momentum operators, and A is the coupling constant. In a high field OPNMR experiment, the enhanced nuclear spin polarization, I_z/I (where $I = 3/2$ for ^{69}Ga and ^{71}Ga), generated by ONP is detected by ordinary nuclear magnetic resonance (NMR) radio wave absorption at the Larmor frequency [11–14]. Hyperpolarization by ONP has facilitated OPNMR studies of nuclei in single sub-30-nm-wide GaAs QWs [11] and arrays of wells [15].

Optical nuclear polarization in bulk GaAs has been modeled by a scalar relaxation mechanism in which electron-nuclear spin exchange transitions are mediated by fluctuations in the Fermi-contact hyperfine coupling [16,17]. The initial rate of ONP buildup in this model is proportional to $S_z - S_{z,\mathrm{eq}}$, i.e., the deviation of the steady-state optically pumped conduction electron spin Zeeman order (which is proportional to the polarization S_z/S) from its thermal equilibrium value [16]. Since S_z is a function of the spin-dependent optical absorption, the photon energy dependence of the OPNMR signal reflects the spin-dependent band structure in both the valence and conduction bands. The complexity of the band structure at high magnetic fields results in a rich structure in the OPNMR photon energy dependence [11,15,18]. Additional complexity is introduced by quantum confinement and strain effects. Here, we use computational modeling to compute the conduction band spin-dependent absorption coefficients. Based on a literature cross-relaxation model appropriate for ONP in n-doped GaAs [18], we simulate the OPNMR photoexcitation energy dependence and compare it to the experimental data.

Optically pumped nuclear magnetic resonance has previously been used to probe the band structure in bulk GaAs [19,20]. In the work of Ramaswamy *et al.* [20], the photon energy dependence of OPNMR signals in bulk GaAs at high magnetic field was interpreted by direct comparison of the data to the spin polarization, S_z/S, calculated from a modified PB model [21]. On this basis, features in the OPNMR energy

*stanton@phys.ufl.edu
†bowers@chem.ufl.edu

dependence were assigned to specific interband LL transitions. The programming code has since been extended to include effects of both quantum confinement and strain.

Simulation of $I_z(h\nu_l)$ requires: (i) a calculation of the absorption coefficients α^+ and α^- for transitions to electron spin-up and spin-down states in the conduction band at a given photon energy and magnetic field, and (ii) an appropriate ONP model relating α^+ and α^- obtained in the band structure calculations to the nuclear spin polarization, I_z/I. In the scalar relaxation model for a spin system consisting of one electron coupled to one $I = 3/2$ nucleus [22,23], ONP at short pumping times (with nuclei initially unpolarized) can be modeled by the term

$$I_z \propto \frac{1}{T_1^{II}}(S_z - S_{z,\mathrm{eq}}) \tag{1}$$

where $1/T_1^{II}$ is the electron-nuclear cross-relaxation rate constant [16,24]. Optical nuclear polarization in quantum confined GaAs appears consistent with nuclear spin hyperpolarization mediated by Fermi-contact interactions [11,15,18,25,26].

In the conduction band of a quantum confined semiconductor at high magnetic field, T_1^{II} could also vary with the electronic state. While different excited states may be accessed as the photoexcitation energy is varied, ONP occurs in the thermalized state. During thermalization of the electronic states, electron spin relaxation may potentially occur by various mechanisms. The Dyakanov-Perel mechanism, which stems from the lifting of the degeneracy of the conduction band when $k \neq 0$ for k-directions other than the principal axes $\langle 100\rangle$ and $\langle 111\rangle$, is effectively suppressed at sufficiently high magnetic field [27,28]. The Elliott-Yafet mechanism [29,30] is expected to be very weak, since the conduction band states are almost pure spin states. Electron scattering by holes, leading to relaxation by the Bir-Aronov-Pikus mechanism [31], is not expected to be significant in our n-type GaAs sample, since, as discussed below, the photocarrier density is significantly less than the doping density. Therefore, we hypothesize that under our experimental conditions, the polarization vector is conserved through the thermalization of the electronic states. The steady-state conduction electron spin polarization depends on the electron spin relaxation time, T_{1s}, and the excited state lifetime, τ_e. If $T_{1s} \ll \tau_e$, electron spins thermally equilibrate (i.e., $S_z \rightarrow S_{z,\mathrm{eq}}$), and no ONP occurs. The observation of strong OPNMR signals in our GaAs QW sample suggests that $T_{1s} > \tau_e$.

We adopt the expression for $S_z - S_{z,\mathrm{eq}}$ derived by Akiba *et al.* [18] for an n-doped GaAs QW under optical pumping conditions:

$$S_z - S_{z,\mathrm{eq}} = \frac{n_l}{n_{\mathrm{eq}} + n_l}\frac{S_z^0 - S_{z,\mathrm{eq}}}{1 + \tau_e/T_{1s}} \tag{2}$$

where n_l is the photoexcited electron density, and n_{eq} is the equilibrium electron density in the absence of optical pumping. The photoexcited electron spin polarization at the instant of optical absorption S_z^0 can be calculated from the energy-dependent spin-up and spin-down absorption coefficients

$$S_z^0 = \frac{1}{2}\frac{\alpha^+ - \alpha^-}{\alpha^+ + \alpha^-}. \tag{3}$$

When $n_l \ll n_{\mathrm{eq}}$ and $T_{1s} > \tau_e$, Eqs. (1) and (2) can be combined to give

$$I_z(h\nu_l) \propto \frac{1}{T_1^{II}}[\alpha^+(h\nu_l) + \alpha^-(h\nu_l)]\left[S_z^0(h\nu_l) - S_{z,\mathrm{eq}}\right] \tag{4}$$

where we have used $n_l \propto \alpha^+ + \alpha^-$. The nuclear spin polarization, $I_z(h\nu_l)/I$, in an OPNMR experiment depends on the laser photon energy $h\nu_l$ through the photon energy dependence of the absorption coefficients. For 200 mW/cm^2 at 1.52 eV, the maximum possible generation rate of photoexcited electrons is $G = 8\times10^{17}$ s^{-1} cm^{-2}. Assuming an electron lifetime of $\tau_e =$ 1 ns [32], the maximum possible steady-state photoexcited electron density is $G\tau_e = 8\times10^8$ cm^{-2}. Thus, the condition $n_l \ll n_{\mathrm{eq}}$ is satisfied for our QW sample, which is δ-doped to a level of $n_{\mathrm{eq}} = 7\times10^{10}$ cm^{-2}. The cross-relaxation rate, $1/T_1^{II}$, is a function of the conduction electron density. For example, in bulk n-doped Si, $1/T_1^{II}$ is linear in n_{eq} for $n_{\mathrm{eq}} > 10^{17}$ cm^{-3} [33]. For our n-doped QWs, where the photoexcited electron density is much lower than the doping density n_{eq}, we will assume $1/T_1^{II}$ to be independent of the optical absorption. In the results presented below, OPNMR signals, which are proportional to $I_z(h\nu_l)$, are compared to the quantity $[\alpha^+(\nu_l) + \alpha^-(\nu_l)][S_z^0(\nu_l) - S_{z,\mathrm{eq}}]$ obtained from the electronic band structure calculations. The comparison facilitates assignment of prominent features in the $I_z(h\nu_l)$ data to specific interband transitions, allowing interpretation of the effects of *strain* and quantum confinement in ONP. We find ONP to be extremely sensitive to relatively small changes in the strain or the pump laser photon energy. Interestingly, multiple changes in the sign of $I_z(h\nu_l)$ are observed over a rather small range of photon energies. These sign changes are related to strain and quantum confinement effects in the electron band structure.

III. EXPERIMENTAL SECTION

A. Equipment and methods

The experiments were performed on a $Al_{0.1}Ga_{0.9}As$/GaAs multiple quantum well (MQW) structure (EA-124; see Fig. 1) consisting of twenty-one 30-nm-wide GaAs wells separated by 360-nm-wide $Al_{0.1}Ga_{0.9}As$ barriers with Si-δ-doping to give a two-dimensional (2D) electron density of 7×10^{10} cm^{-2}. To eliminate background NMR signals due to the GaAs growth substrate, EA-124 was epoxy bonded to a Si single crystal support, and the growth substrate was removed by selective chemical etching following the epoxy bond and stop-etch (EBASE) technique [34]. Upon cooling the sample to low temperature, differential thermal contraction between the sample and substrate resulted in a uniform biaxial tensile strain in the film, as discussed in detail below. Unless otherwise stated, the static magnetic field was applied parallel to both the $\langle 100\rangle$ QW growth direction and the direction of electronic confinement.

A copper NMR coil was wound in a rectangular shape with dimensions slightly larger than the sample. Coil windings were placed into grooves cut into the face of a sapphire block and were fixed in place using GE varnish. To mitigate sample heating due to laser irradiation, the sample was mounted in physical contact with the sapphire block inside the NMR coil using Apiezon N grease. The sapphire block was mounted into a homebuilt NMR probe, and the NMR coil was incorporated into a tank circuit that could be impedance matched to 50 Ohms

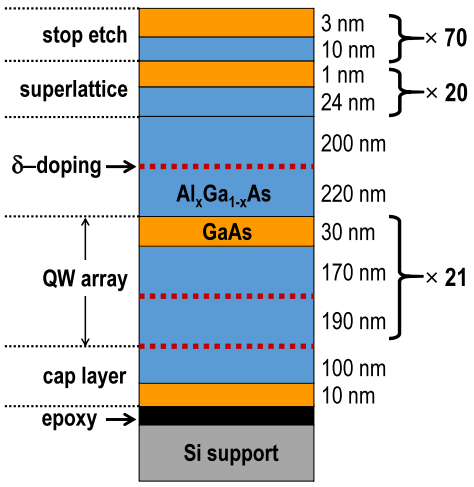

FIG. 1. (Color online) Schematic structure of EA-124, which is composed of layers of GaAs (orange), $Al_xGa_{1-x}As$ (blue), and Si-δ-doping (red dashed lines). The Si-δ-doping level is 4×10^{11} cm^{-2} for the bottom dashed line and 2×10^{11} cm^{-2} for middle and top dashed lines. The Al composition is $x = 0.1$ in the MQW layers, $x = 0.1 \rightarrow 0.55$ in the superlattice layers, and $x = 0.55$ in the stop etch layers. Thicknesses of each layer are specified to the right of the structure along with the repeat multiple. The entire structure is epoxy-bonded (black) to a Si support (gray).

and tuned to the nuclear Larmor frequency of the nucleus of interest at low temperature. At the experimental temperature, the Q-factor of the circuit was measured to be 70.

Experiments were performed at a series of different magnetic fields ranging from 3.0 to 9.4 T. For experiments above 3.0 T, the probe was lowered into a 0–17 T variable superconducting cold bore magnet. After inserting the probe into the cold bore, a low-pressure (∼5 mbar) helium exchange gas was introduced into the bore of the magnet, allowing heat exchange with the magnet's liquid helium dewar, to cool the probe and the sample to 4.2 K. The temperature of the sample space was monitored by a Lakeshore Cernox CX-1030 temperature sensor that was mounted approximately 2 cm from the sample.

Optically pumped nuclear magnetic resonance experiments performed at the National High Magnetic Field Laboratory (NHMFL) utilized a Coherent Verdi V5 pumped Coherent Mira 900 Ti:Sapphire laser with a 0.35 meV line width operated in continuous wave mode for all experiments. Laser light from the Ti:Sapphire laser was directed through polarization optics, a polarizing beam splitting cube, and a zero-order quarter-wave plate centered at 800 nm, and into the bore of the magnet through an optical window. Optical power was measured using an Ophir Photonics thermopile detector (P/N 7Z02621) and controlled using a variable neutral density filter. Photon energy was measured using a McPherson 0.75 m pathlength monochromator equipped with a 600 grooves/mm grating and a Princeton Instruments charge-coupled device (CCD) (Model No. IN/CCD-1024-UV). For an entrance slit width of 20 μm, the energy resolution of the setup was 0.1 meV at 1530.7 meV.

Nuclear magnetic resonance spectra were acquired at the NHMFL using a homebuilt spectrometer. Individual OPNMR spectra were acquired using a standard saturation-recovery pulse sequence with continuous laser irradiation for the entirety of the pulse sequence. A fixed irradiation time of 120 s was used in all experiments. At a given magnetic field, OPNMR spectra were acquired as the photon energy and polarization were varied. This was repeated at several different magnetic field strengths.

Additional experiments were conducted at 3.0 T and 9.4 T using an Oxford Instruments CF-1200 continuous flow cryostat inserted into the bore of the high-homogeneity, room-temperature, 89-mm-bore superconducting magnets. These studies utilized a Coherent Verdi G 15 W pumped Coherent 899 Ti:Sapphire laser as an energy tunable photon source. The output beam of the Ti:Sapphire laser was focused into a 600-μm-core-diameter fiber optic, which terminated directly above the sample. Optical power was measured using a Coherent Field Master power meter with a Coherent LM10 detector and controlled using a variable neutral density filter. Photon energy was measured using an Ocean Optics USB2000 spectrometer with an 1800 grooves/mm grating and an entrance slit width of 5 μm, giving an energy resolution of 0.4 meV at 1530.7 meV. The NMR probe was fitted with a sample rotation stage incorporating a worm/worm gear pair with a 30:1 reduction for variable tilt angle experiments.

B. Theory

The model used here incorporates: (i) quantum confinement effects in the EA-124 QW structure; (ii) *strain* that arises from differential thermal contraction between the GaAs/$Al_{0.1}Ga_{0.9}As$ film and the Si support to which the film is bonded; and (iii) the interaction with the applied magnetic field. The calculations are based on an eight-band PB model that was modified and extended to include the effects of quantum confinement and strain. A similar model was used previously to study cyclotron resonance in the dilute magnetic semiconductors InMnAs [10] and cyclotron resonance and magneto-absorption in InSb [21,35,36] and InMnSb [37]. Since details are explained in Ref. [10], only the salient features of this model as it applies to the strained EA-124 QW structure are outlined here. We use the PB model in the *axial* approximation. In this approximation, the Luttinger parameters γ_2 and γ_3 are set equal to each other. This allows us to neglect the coupling between PB manifolds and solve each one individually, which greatly aids in the calculation. The effective mass Hamiltonian is written as

$$H = H_L + H_Z + H_S + H_C \tag{5}$$

where H_L is the Landau Hamiltonian [10], H_Z is the Zeeman Hamiltonian, and H_C is the confinement Hamiltonian, which results from differences in the band gap between the wells and barriers. The strain Hamiltonian H_S is given by [38–40]

$$H_S = \begin{bmatrix} S_a & S_c \\ S_c^\dagger & S_b \end{bmatrix} \tag{6}$$

where

$$S_a = \begin{bmatrix} A_\varepsilon & 0 & 0 & 0 \\ 0 & -P_\varepsilon - Q_\varepsilon & -M_\varepsilon & i\sqrt{2}M_\varepsilon \\ 0 & -M_\varepsilon^* & -P_\varepsilon + Q_\varepsilon & i\sqrt{2}Q_\varepsilon \\ 0 & -i\sqrt{2}M_\varepsilon^* & -i\sqrt{2}Q_\varepsilon & -P_\varepsilon \end{bmatrix} \quad (7)$$

$$S_b = \begin{bmatrix} A_\varepsilon & 0 & 0 & 0 \\ 0 & -P_\varepsilon - Q_\varepsilon & -M_\varepsilon^* & i\sqrt{2}M_\varepsilon^* \\ 0 & -M_\varepsilon & -P_\varepsilon + Q_\varepsilon & i\sqrt{2}Q_\varepsilon \\ 0 & -i\sqrt{2}M_\varepsilon & -i\sqrt{2}Q_\varepsilon & -P_\varepsilon \end{bmatrix} \quad (8)$$

$$S_c = \begin{bmatrix} 0 & 0 & 0 & 0 \\ 0 & 0 & -L_\varepsilon & -i\sqrt{\frac{1}{2}}L_\varepsilon \\ 0 & L_\varepsilon & 0 & i\sqrt{\frac{3}{2}}L_\varepsilon^* \\ 0 & -i\sqrt{\frac{1}{2}}L_\varepsilon & i\sqrt{\frac{3}{2}}L_\varepsilon^* & 0 \end{bmatrix} \quad (9)$$

and

$$A_\varepsilon = a_c(\varepsilon_{xx} + \varepsilon_{yy} + \varepsilon_{zz}) \quad (10)$$

$$P_\varepsilon = -a_v(\varepsilon_{xx} + \varepsilon_{yy} + \varepsilon_{zz}) \quad (11)$$

$$Q_\varepsilon = -\frac{b}{2}(\varepsilon_{xx} + \varepsilon_{yy} - 2\varepsilon_{zz}) \quad (12)$$

$$M_\varepsilon = -\frac{\sqrt{3}}{2}b(\varepsilon_{xx} - \varepsilon_{yy}) + i\frac{2\sqrt{3}}{3}d\varepsilon_{xy} \quad (13)$$

and

$$L_\varepsilon = id(\varepsilon_{xz} - i\varepsilon_{yz}). \quad (14)$$

Here, ε_{ij} are the components of the strain tensor, and a_c, a_v, b, and d are deformation potentials, which for GaAs can be found in Ref. [41]. For the case of biaxial tensile strain, $\varepsilon_{xx} = \varepsilon_{yy}$ and $\varepsilon_{ij} = 0$ for $i \neq j$, giving $M_\varepsilon = L_\varepsilon = 0$. Hence,

$$S_a = S_b = \begin{bmatrix} A_\varepsilon & 0 & 0 & 0 \\ 0 & -P_\varepsilon - Q_\varepsilon & 0 & 0 \\ 0 & 0 & -P_\varepsilon + Q_\varepsilon & i\sqrt{2}Q_\varepsilon \\ 0 & 0 & -i\sqrt{2}Q_\varepsilon & -P_\varepsilon \end{bmatrix} \quad (15)$$

and

$$S_c = 0. \quad (16)$$

To model quantum confinement effects in the QW structure with an effective mass Hamiltonian, we replace the z component of the wave vector k_z with a differential operator $k_z \rightarrow -i\,\nabla_z$ along the confinement direction ($\hat{z}$). We then divide the superlattice unit cell into G equally spaced grid points, so that the ∇_z operator can be approximated by finite differences on the grid. In addition, all the material parameters are allowed to vary with position along $\hat{z}$. We use a finite difference approach on each PB manifold, allowing us to calculate all the LLs for each quantum confined subband. However, this increases the size of the matrix to be diagonalized from 8×8 (size of the effective mass Hamiltonian matrix without grid points) to $8G \times 8G$. In the present paper, we chose $G = 101$. The 808×808 matrix is diagonalized numerically to obtain Landau subband energies and corresponding wave functions. Increasing the number of grid points did not significantly change the calculated band structure.

We solved the eigenvalue equations [10]

$$H_p F_{p,v} = E_{p,v}(k_z) F_{p,v} \quad (17)$$

for the eigenvalues and eigenvectors using the eight Bloch basis states consisting of the spin-up/spin-down conduction band (*CB*), light hole (*LH*), heavy hole (*HH*), and split-off hole (*SO*) states. In Eq. (17), p is the PB manifold index and has allowed values of $p \geqslant -1$, while v labels the eigenstates in the p^{th} manifold in ascending order. Solutions are labeled as $BS^p_{sb}\uparrow$, where BS corresponds to the Bloch basis state (see above), which dominates the character of the eigenvector, p is the PB manifold index, sb is the subband number, and the arrow indicates the "spin state" of the Bloch basis state. Note that "spin-up" and "spin-down" correspond to the maximum and minimum m_j values for the type of basis state. For instance,

$$|HH\uparrow\rangle = \left|j = \tfrac{3}{2};\ m_j = \tfrac{+3}{2}\right\rangle \quad \text{is the } HH \text{ up state; and}$$

$$|LH\downarrow\rangle = \left|j = \tfrac{3}{2};\ m_j = \tfrac{-1}{2}\right\rangle \quad \text{is the } LH \text{ down state.}$$

We note that $|HH\uparrow\rangle$ is a *pure* spin state (i.e., eigenstate of S_z), while $|LH\downarrow\rangle$ is not a *pure* spin state. It is important to note that the PB manifold number is *not* the same as the LL number. Within a given PB manifold, the LL number depends on the basis state. For instance, by looking at Eq. (27) of Ref. [10], we see that in the p^{th} PB manifold, the *HH* down state is in the $p+1$ LL harmonic oscillator state, while the *CB* up state is in the $p-1$ state, and the *LH* down state is in the p state, etc. The LL number n can be calculated from the PB index p using the relations listed in Table I. We note that, while within a given PB manifold, the sum of the n and the m_j quantum number of the Bloch basis state is a constant given by $n + m_j = p - 1/2$.

At a magnetic field B_z, the photon energy–dependent absorption coefficients, $\alpha(h\nu_l)$, are obtained from the imaginary part of the dielectric function, which is calculated using Fermi's golden rule [10]. The absorption coefficient is given by

$$\alpha(h\nu_l) = \frac{e^3 B_z}{h\nu_l(\hbar c)^2 n_r} \sum_{p,v,p',v'} \int_{-\infty}^{\infty} dk_z \left|\hat{e} \cdot \vec{P}^{p',v'}_{p,v}(k_z)\right|^2 \times (f_{p,v}(k_z) - f_{p',v'}(k_z))\delta\left(\Delta E^{p,v}_{p',v'}(k_z) - h\nu_l\right) \quad (18)$$

where n_r is the index of refraction, $\hat{e} \cdot \vec{P}^{p',v'}_{p,v}$ are the optical matrix elements (see Ref. [10]), $f_{p,v}$ is the Fermi distribution,

TABLE I. Relationship between PB index p and LL number n for the given basis states.

Basis State	Relation
$CB\uparrow$	$n = p - 1$
$CB\downarrow$	$n = p$
$LH\uparrow$	$n = p - 1$
$LH\downarrow$	$n = p$
$HH\uparrow$	$n = p - 2$
$HH\downarrow$	$n = p + 1$
$SO\uparrow$	$n = p - 1$
$SO\downarrow$	$n = p$

$\hat{e}$ is the optical polarization vector, and $\Delta E^{p,v}_{p',v'}$ is the optical transition energy. Separate absorption coefficients were calculated for transitions generating spin-up and spin-down *CB* electrons. This was accomplished by limiting the sum in Eq. (18) to just one of the given *CB* spins. (We note that the *CB*–valence band mixing in GaAs is weak, and, as a result, the *CB* LLs are over 99% of a given spin type.) Using these spin-dependent absorption coefficients, the energy dependence of $S_z^0 - S_{z,\mathrm{eq}}$ can be calculated using Eq. (3), and the energy dependence of $I_z(h\nu_l)$ can be calculated using Eq. (4). Within the axial approximation, absorption of σ^+ circularly polarized light occurs only between PB manifolds that differ by $+1$; i.e., $p \rightarrow p+1$ is the selection rule for σ^+ polarized light. For σ^- circularly polarized light, the selection rule is $p \rightarrow p-1$.

IV. RESULTS AND DISCUSSION

Figure 2 shows the thermally polarized and optically pumped Ga-71 NMR spectra of EA-124 at 4.2 K and 9.4 T. Upon cooling, strain is induced due to differential contraction of the MQW film and the Si support to which it is epoxy bonded. Due to Poisson's law, the biaxial tensile strain in the plane of the sample (the xy-plane) produces an associated strain along the z axis, ε_{zz}. Strain along the z axis produces an electric field gradient (EFG) along the z axis, V_{zz}, leading to a quadrupole splitting of the nuclear spin states, which has been previously reported in the OPNMR spectrum of EA-124 [15].

The *thermally* polarized NMR spectrum exhibits a single line because it is dominated by the NMR signal from nuclei located in the $Al_xGa_{1-x}As$ regions of the structure; >90% of Ga nuclei are in $Al_xGa_{1-x}As$ regions of EA-124. The single resonance in the thermally polarized spectrum is assigned to the central transitions of $Al_xGa_{1-x}As$. Satellite transitions from the $Al_xGa_{1-x}As$ barriers are not observed due to first-order quadrupole broadening resulting from the alloy disorder in the $Al_xGa_{1-x}As$ material. Similar observations are reported

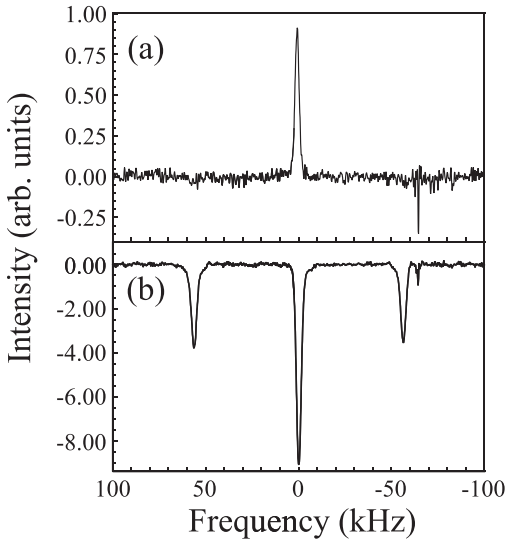

FIG. 2. (a) Thermally polarized ^{71}Ga NMR spectrum of EA-124 at 4.2 K and 9.4 T acquired immediately after cooling the sample. (b) ^{71}Ga OPNMR spectrum of EA-124 at 4.2 K, acquired using $\tau_{\mathrm{ONP}} = 50$ s.

for $Al_xGa_{1-x}As$ for $x = 0.1$ [42] and $x = 0.5$ [43]. Because optical absorption occurs only within the GaAs QW, ONP hyperpolarizes nuclear spins *in the QW region*. The nuclear spin hyperpolarization diffuses from the QW nuclei into the $Al_{0.1}Ga_{0.9}As$ barriers of EA-124. Thus, our OPNMR spectrum contains signal contributions from both the GaAs QWs and the $Al_{0.1}Ga_{0.9}As$ barriers. As previously reported, *nuclei in the QW region* of EA-124 exhibit a strain-induced nuclear quadrupole splitting, which is observable because (i) ONP produces large NMR signal enhancements, and (ii) there is no alloy disorder within the well [15]. The central and satellite transitions in the OPNMR spectrum in Fig. 2(b) are in phase. The linear phase correction applied to obtain the spectrum in Fig. 2(b) was validated by setting the spectrometer frequency on resonance with each of the three transitions and then applying the same zero-order phase correction as was applied to the thermally polarized signal.

Using the quadrupole moment of the nucleus and the observed quadrupole splitting in the OPNMR spectrum, we obtain $V_{ZZ} = 1.45\times10^{13}\,\mathrm{erg\cdot stat\,C^{-1}\cdot cm^{-2}}$ and $\varepsilon_{zz} = -7.7\times10^{-4}$ from the Ga-71 OPNMR spectrum (see Appendix). Similarly, $V_{ZZ} = 1.25\times10^{13}\,\mathrm{erg\cdot stat\,C^{-1}\cdot cm^{-2}}$ and $\varepsilon_{zz} = -6.6\times10^{-4}$ are obtained from the Ga-69 OPNMR spectrum. To validate our calculation of ε_{zz}, we compared the strain in EA-124 to that of a 1.1-μm-thick GaAs epitaxial liftoff (ELO) sample bonded to Si [44]. Photoluminescence measurements from the ELO sample reveal a valence band splitting (between the *LH* and *HH*) of 4.2 meV. To relate the valence band splitting to strain, we used equations for the transition energy, to first order, of the *LH*-to-*CB*, ΔE_{lh}, and *HH*-to-*CB*, ΔE_{hh}, under biaxial strain, $\varepsilon = \varepsilon_{xx} = \varepsilon_{yy}$, which are [45,46]

$$\Delta E_{lh} = \left(-2a\frac{C_{11}-C_{12}}{C_{11}} + b\frac{C_{11}+2C_{12}}{C_{11}}\right)\varepsilon \tag{19}$$

and

$$\Delta E_{hh} = \left(-2a\frac{C_{11}-C_{12}}{C_{11}} - b\frac{C_{11}+2C_{12}}{C_{11}}\right)\varepsilon. \tag{20}$$

Thus, the relationship between the valence band splitting, $\Delta E_{lh} - \Delta E_{hh}$, and ε is

$$\Delta E_{lh} - \Delta E_{hh} = 2b\frac{C_{11}+2C_{12}}{C_{11}}\varepsilon. \tag{21}$$

Using values of $12.1\times10^{12}\,\mathrm{dynes\,cm^{-2}}$ [47], $5.48\times10^{12}\,\mathrm{dynes\,cm^{-2}}$ [47], and -2.0 eV [48] for C_{11}, C_{12}, and b, respectively, we find that a strain of $\varepsilon = 5.5\times10^{-4}$ would produce a 4.2 meV valence band splitting. Finally, ε_{zz} is given by [45]

$$\varepsilon_{zz} = -\frac{2C_{12}}{C_{11}}\varepsilon. \tag{22}$$

Using Eq. (22), we calculate $\varepsilon_{zz} = -5.0\times10^{-4}$ in the ELO sample. The slightly smaller value of ε_{zz} in the ELO sample is expected because it was bonded to Si at room temperature, while EA-124 was bonded to Si at a temperature of 100 °C. The slightly higher bonding temperature results in a larger strain upon cooling the sample.

The strain estimated from the quadrupole splitting ($\varepsilon_{zz} = -7\times10^{-4}$) was used as input into the calculations of the

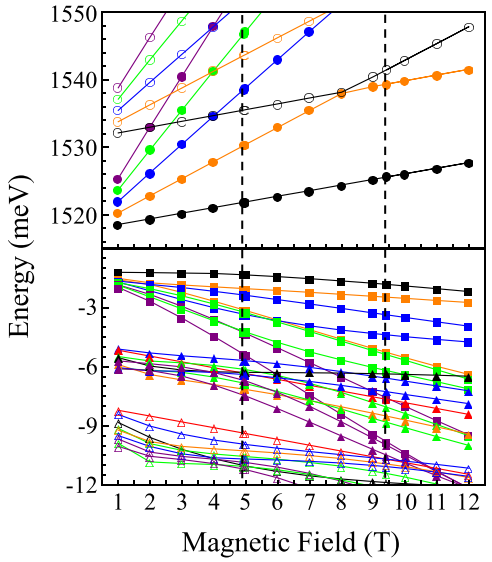

FIG. 3. (Color online) Calculated magnetic field dependence of conduction band (top) energies for CB_1 (•) and CB_2 (○) and the valence band (bottom) energies for LH_1 (■), HH_1 (▲), and HH_2 (△) in EA-124. The dashed vertical lines are 4.9 T and 9.4 T. Colors correspond to PB indices of −1 (red), 0 (black), 1 (orange), 2 (blue), 3 (green), and 4 (purple).

magnetic-field dependence of the band structure from 1 to 12 T (see Fig. 3). Only the CB_1, CB_2, LH_1, HH_1, and HH_2 subbands are displayed because they contribute most significantly to the optically pumped electron spin polarization. First, we note that the gap between the valence and conduction bands is 1519.8 meV at 1 T. There are three different contributions that shift the gap in different directions. Tensile strain narrows the gap. By comparing calculations with and without strain, we estimate this contribution to be about 5 meV in our sample. Conversely, both confinement and magnetic field increase the gap. Because the gap at 1 T is only slightly larger than that of bulk GaAs, the combination of confinement and magnetic field effects is estimated to be slightly larger in magnitude than that of strain.

Next, we note that as expected in the case of tensile strain, the LH_1 states are higher in energy than the HH_1 states. At 1 T, the valence band splitting is about 3.9 meV. This value is smaller than would be expected due to strain alone and is likely due to different quantum confinement shifts for the LH_1 states as compared to the HH_1 states. At 1 T, we also observe a 13.6 meV splitting between CB_1^0 and CB_2^0 and a 3.0 meV splitting between HH_1^{-1} and HH_1^{-2}, which are predominantly due to quantum confinement. The different splittings at 1, 4.9, and 9.4 T are summarized in Table II.

Note that the Coulomb interaction was not included in the band structure calculations. While a thorough treatment of Coulomb effects in strained and doped QWs in a magnetic field is beyond the scope of the present work, we briefly discuss some expected effects of the Coulomb interaction on a qualitative level. The Coulomb interaction between the photoexcited electrons and holes leads to exciton formation. For excitons in bulk GaAs in a magnetic field B_z, Coulombic interactions produce a shift in the absorption edge that depends on the ratio of the cyclotron and Coulomb binding energies,

TABLE II. Summary of relevant energy splittings determined from the calculated band structure of EA-124 for fields of 1, 4.9, and 9.4 T. Energies are given in meV.

	1 T	4.9 T	9.4 T
		Gap	
$LH_1^0 \rightarrow CB_1^0$	1519.8	1523.3	1527.4
		Confinement	
$CB_1^0 \rightarrow CB_2^0$	13.6	13.7	15.9
$HH_1^{-1} \rightarrow HH_2^{-1}$	3.7	3.7	4.1
		Strain	
$LH_1^0 \rightarrow HH_1^{-1}$	3.9	4.3	4.8

2β, with [49]

$$\beta = \frac{\varepsilon^2 \hbar^2 B_z}{\mu^2 e^3 c} \tag{23}$$

where ε is the absolute permittivity, $\hbar$ is the reduced Planck's constant, μ is the reduced mass of the exciton, e is the electron charge, and c is the speed of light. Though EA-124 is quite different than bulk GaAs, we expect that at 4.9 T, we are in a regime of $\beta > 1$, where magnetic effects begin to exceed Coulomb effects. Typical exciton binding energies in bulk GaAs are about 5 meV. In a quantum confined system at high magnetic field, the exciton binding energies can be larger. In our current system, strain changes the ordering of the heavy and light hole energies, further complicating calculation of exciton binding energy. More work is required to quantitatively evaluate β and solve for the shift in the absorption edge in EA-124. To account for Coulombic shifts of the absorption edge at a given magnetic field, the entire energy scale of the absorption coefficient calculations was shifted by a fixed amount. We have neglected any dependence of Coulombic effects on the LL number, though in a real system, this can be important. Coulombic effects are expected to be strongest near the absorption edge and become weaker at higher photon energies.

The dependence of the OPNMR signal (the peak area of the central transition) on photon energy for σ^- and σ^+ light at 4.9 T is plotted in Fig. 4. In the top panels, $I_z(h\nu_{\text{laser}})$ obtained using Eq. (4) and S_z^0 are superimposed on the experimental OPNMR data. The bottom panels present the PB manifold-resolved (i.e., separated by transitions from p to p') absorption coefficients, also at 4.9 T. This aids us in identifying the transitions. The energy scale for the calculations at 4.9 T is shifted by 13.7 meV. Prominent features are labeled according to the transition that dominates at that energy. The transitions are summarized in Table III, along with the subbands involved in each transition and the composition of the states in terms of the eight Bloch basis states (i.e., the band mixing). For $\mathbf{T_6}$ with σ^- polarization, the spin label is omitted because the transition results from the $HH\uparrow$ character of the initial state, even though it is predominantly a $LH\downarrow$ state.

The calculated absorption coefficients vary rapidly with photon energy in a strained QW at high field, which explains

TABLE III. Transitions, labels, subband labels, and wave function probabilities for 4.9 T.

	Transition	Label	Subband Label	Wave Function Probability
	T_1	$LH_1^1\uparrow \rightarrow CB_1^0\downarrow$	$LH_1^1\uparrow$	89% $LH\uparrow$ + 8% $HH\downarrow$
			$CB_1^0\downarrow$	99.6% $CB\downarrow$
	T_2	$HH_1^2\uparrow \rightarrow CB_1^1\uparrow$	$HH_1^2\uparrow$	33% $HH\uparrow$ + 15% $HH\downarrow$ + 13% $LH\downarrow$ + 38% $LH\uparrow$
			$CB_1^1\uparrow$	99.7% $CB\uparrow$
	T_3	$LH_1^2\uparrow \rightarrow CB_1^1\downarrow$	$LH_1^2\uparrow$	77% $LH\uparrow$ + 13.3% $HH\uparrow$
			$CB_1^1\downarrow$	99% $CB\downarrow$
σ^-	T_4	$HH_1^3\uparrow \rightarrow CB_1^2\uparrow$	$HH_1^3\uparrow$	35% $HH\uparrow$ + 57% $LH\downarrow$
			$CB_1^2\uparrow$	99% $CB\uparrow$
	T_5	$HH_1^2\uparrow \rightarrow CB_2^1\uparrow$	$HH_1^2\uparrow$	33% $HH\uparrow$ + 15% $HH\downarrow$ + 13% $LH\downarrow$ + 38% $LH\uparrow$
		and	$CB_2^1\uparrow$	99% $CB\uparrow$
		$LH_1^3\uparrow \rightarrow CB_1^2\downarrow$	$LH_1^3\uparrow$	74% $LH\uparrow$ + 15% $HH\uparrow$
			$CB_1^2\downarrow$	98.8% $CB\downarrow$
	T_6	$LH_1^4 \rightarrow CB_1^3\uparrow$	LH_1^4	53.5% $LH\downarrow$ + 36.7% $HH\uparrow$
			$CB_1^3\uparrow$	99% $CB\uparrow$
	T_1	$LH_1^0\downarrow \rightarrow CB_1^1\uparrow$	$LH_1^0\downarrow$	92% $LH\downarrow$
			$CB_1^1\uparrow$	99% $CB\uparrow$
	T_2	$HH_1^{-1}\downarrow \rightarrow CB_1^0\downarrow$	$HH_1^{-1}\downarrow$	100% $HH\downarrow$
			$CB_1^0\downarrow$	99.6% $CB\downarrow$
	T_3	$LH_1^1\downarrow \rightarrow CB_1^2\uparrow$	$LH_1^1\downarrow$	85% $LH\downarrow$ + 14% $HH\downarrow$
			$CB_1^2\uparrow$	99.3% $CB\uparrow$
σ^+	T_4	$HH_1^0\downarrow \rightarrow CB_1^1\downarrow$	$HH_1^0\downarrow$	45% $HH\downarrow$ + 54% $LH\downarrow$
			$CB_1^1\downarrow$	99% $CB\downarrow$
	T_5	$HH_2^0\downarrow \rightarrow CB_1^1\downarrow$	$HH_2^0\downarrow$	71% $HH\downarrow$ + 28% $LH\downarrow$
		and	$CB_1^1\downarrow$	99% $CB\downarrow$
		$LH_1^2\downarrow \rightarrow CB_1^3\uparrow$	$LH_1^2\downarrow$	58.5% $LH\downarrow$ + 34.5% $HH\uparrow$
			$CB_1^3\uparrow$	99% $CB\uparrow$
	T_6	$HH_2^{-1}\downarrow \rightarrow CB_2^0\downarrow$	$HH_2^{-1}\downarrow$	100% $HH\downarrow$
			$CB_2^0\downarrow$	99% $CB\downarrow$

the rapid oscillations in $I_z(h\nu_l)$. Reasonably good agreement is obtained between theory and experiment, particularly in the predicted positions of the maxima and minima. However, not all features in the data are captured by the theory. With increasing photon energy, the amplitude of the oscillations in the calculated $I_z(h\nu_l)$ steadily increases, while in the data these oscillations are damped. At the higher photon energies, the data show a closer match to S_z^0. This might be due to one or more of the following factors: penetration depth effects, nonlinear dependence of the OPNMR signal with absorption at some photon energies, and effects of sample heating (such as reduction of T_{1s} and/or τ_e).

The OPNMR photon energy dependence data and corresponding calculations at 9.4 T are shown in Fig. 5. The energy scale for all calculated quantities has been shifted by 16.1 meV. The increase in the shift, compared to 4.9 T, reflects larger Coulombic effects at a higher magnetic field. The dominant transitions at 9.4 T are listed in Table IV, along with the subbands involved in the transitions and their decomposition in terms of probability densities of the basis states. Similar to the 4.9 T data, there are several transitions ($\mathbf{T_2}$ and $\mathbf{T_3}$ for σ^- and $\mathbf{T_3}$ for σ^+) where the spin label has been omitted from the valence band subband descriptor because the transition involves the eigenstate with a spin state that differs from that of the dominant eigenstate in the linear combination.

Our results show that the OPNMR photon energy dependence is highly sensitive to both confinement and strain effects. For example, at 4.9 T, the $\mathbf{T_2}$ and $\mathbf{T_6}$ for σ^+ excitation and $\mathbf{T_2}$ and $\mathbf{T_5}$ for σ^- excitation involve transitions to different confinement subbands of the conduction band. An obvious effect of strain is that *the lowest energy transition for both polarizations of light is from a LH initial state*. In the absence of strain, the lowest energy transition would be expected to originate from a *HH* initial state.

Strain effects are seen to be significant in EA-124, producing a LH/HH splitting of $\sim$4 meV. This is noteworthy because, near the band edge in unstrained bulk GaAs in zero magnetic field, the LH/HH degeneracy limits S_z to $S_z = \pm 1/4$

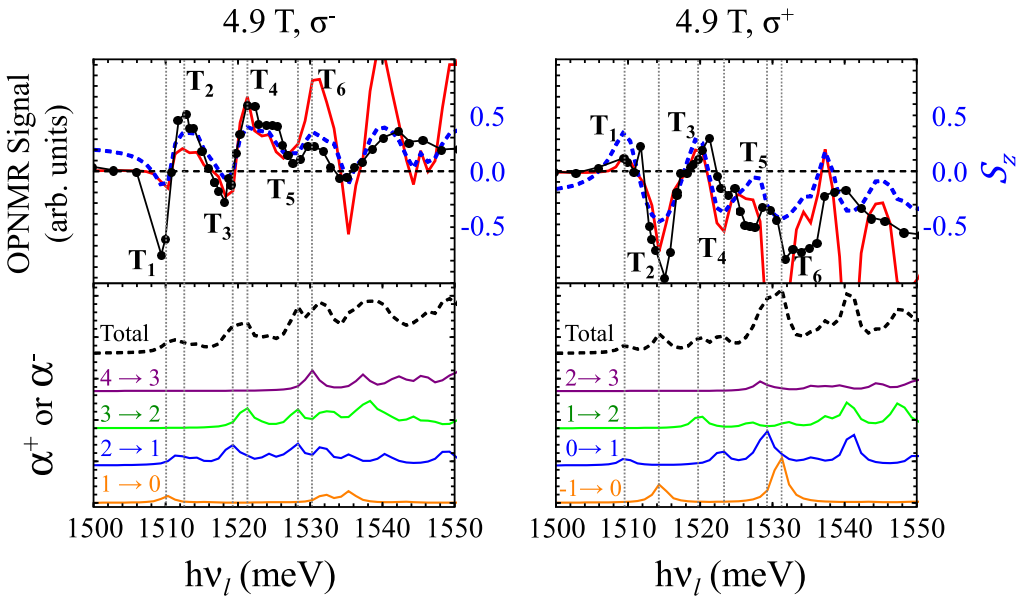

FIG. 4. (Color online) Upper panels: Photon energy dependence of the experimental OPNMR data T = 5.1 ± 0.3 K (black points, arbitrary units), $I_z(h\nu_l)$ calculated using Eq. (4) (red curve, arbitrary units), and S_z^0 (dashed blue curve) at 4.9 T for σ^- and σ^+ light. Lower panels: Decomposition of the total optical absorption coefficients according to PB manifold, as indicated. Gray dotted vertical lines mark prominent features in the data, which are labeled according to transition, T_i.

[14], which in turn limits the maximum achievable nuclear spin polarization. In the case of EA-124, our calculations show that it is possible to selectively excite a *LH* or *HH* to *CB* transition, resulting in fully spin polarized optically pumped electrons. Furthermore, these calculations reveal that the optically pumped S_z can be switched from $S_z^0 = +1/2$ to $S_z^0 = -1/2$ with a change in photon energy of less than 6 meV at 9.4 T. To demonstrate the effect of strain on the photon energy dependence of electron S_z, Fig. 6 presents a plot of S_z versus photon energy for seven different values of strain for EA-124 at 4.9 T. The calculations show that increasing the tensile strain shifts $S_z(h\nu_l)$ to lower energies and results in more pronounced features and larger oscillations in S_z with photon energy.

In Fig. 7, we compare the photon energy dependence of OPNMR signals from EA-124 to that of a bulk GaAs sample. Comparison of the photon energy dependence of these two samples demonstrates the dramatic difference

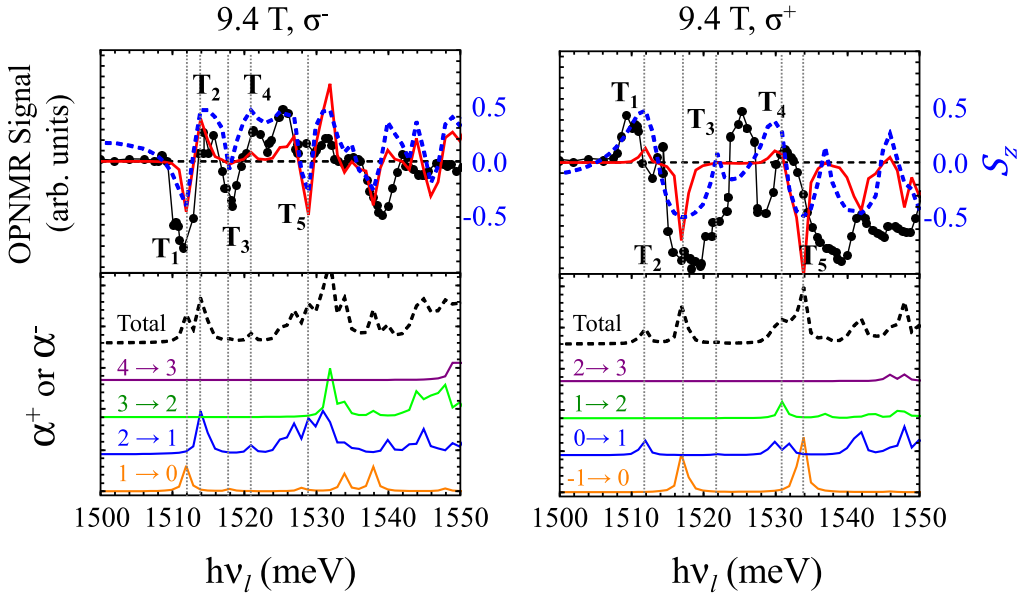

FIG. 5. (Color online) Upper panels: Photon energy dependence of experimental OPNMR data at T = 5.1 ± 0.3 K (black points, arbitrary units), $I_z(h\nu_l)$ calculated using Eq. (4) (red curve, arbitrary units), and S_z^0 (blue dashed curve) at 9.4 T for σ^- and σ^+ light. Lower panels: Decomposition of the total optical absorption coefficients according to PB manifold, as indicated. Gray dotted vertical lines mark prominent features in the data, which are labeled according to transition, T_i.

TABLE IV. Transitions, labels, subband labels, and wave function probabilities for 9.4 T.

	Transition	Label	Subband Label	Wave Function Probability
	T_1	$LH_1^1\uparrow \rightarrow CB_1^0\downarrow$	$LH_1^1\uparrow$	86% $LH\uparrow$ + 10% $HH\downarrow$
			$CB_1^0\downarrow$	99.4% $CB\downarrow$
	T_2	$LH_1^2 \rightarrow CB_1^1\uparrow$	LH_1^2	58% $HH\uparrow$ + 28% $LH\downarrow$ + 14% $LH\uparrow$
			$CB_1^1\uparrow$	99.8% $CB\uparrow$
σ^-	T_3	$HH_1^1 \rightarrow CB_1^0\downarrow$	HH_1^1	60% $LH\downarrow$ + 30% $HH\downarrow$ + 9% $LH\uparrow$
			$CB_1^0\downarrow$	99.4% $CB\downarrow$
	T_4	$HH_2^2\uparrow \rightarrow CB_1^1\uparrow$	$HH_2^2\uparrow$	48% $HH\uparrow$ + 30% $LH\downarrow$ + 20% $HH\downarrow$
			$CB_1^1\uparrow$	99.5% $CB\uparrow$
	T_5	$LH_1^1\uparrow \rightarrow CB_1^1\downarrow$	$LH_1^1\uparrow$	69% $LH\uparrow$ + 23% $HH\uparrow$ + 7.5% $CB\downarrow$
			$CB_1^1\downarrow$	98.7% $CB\downarrow$
	T_1	$LH_1^0\downarrow \rightarrow CB_1^1\uparrow$	$LH_1^0\downarrow$	92% $LH\downarrow$ + 8% $HH\downarrow$
			$CB_1^1\uparrow$	99.5% $CB\uparrow$
	T_2	$HH_1^{-1}\downarrow \rightarrow CB_1^0\downarrow$	$HH_1^{-1}\downarrow$	100% $HH\downarrow$
			$CB_1^0\downarrow$	99.4% $CB\downarrow$
σ^+	T_3	$HH_2^0 \rightarrow CB_1^1$	HH_2^0	44% $LH\downarrow$ + 56% $HH\downarrow$
			CB_1^1	98.8% $CB\uparrow$
	T_4	$LH_1^1\downarrow \rightarrow CB_1^2\uparrow$	$LH_1^1\downarrow$	74% $LH\downarrow$ + 17% $HH\downarrow$
			$CB_1^2\uparrow$	98.8% $CB\downarrow$
	T_5	$HH_2^{-1}\downarrow \rightarrow CB_2^0\downarrow$	$HH_2^{-1}\downarrow$	100% $HH\downarrow$
			$CB_2^0\downarrow$	99% $CB\downarrow$

between the band structure of a strained and quantum confined semiconductor and that of a bulk semiconductor. Notably, no inversions of the signal in the bulk material are observed, indicating that in the case of bulk GaAs, the optically pumped electron spin polarization is always less than the thermal equilibrium electron spin polarization. This is in contrast to the data acquired from EA-124, where multiple signal inversions are observed, indicating that the sign of $S_z^0(h\nu_l) - S_{z,\mathrm{eq}}$ can be reversed. The difference between the bulk (unconfined) semiconductor and the quantum confined semiconductor can be attributed to a fundamental difference in the density of states of the 2D and three-dimensional (3D) systems in high magnetic field. In the 3D system, k_z is a good quantum number. As a result, in 3D systems, the *HH* density of states and *LH* density of states overlap due to the tail extending to the continuum in k_z. On the other hand, the density of states in the 2D system is fully discrete, which allows the pumping of transitions from the *HH* and *LH* bands to be resolved, resulting in an inversion in the sign of the electron spin polarization.

Finally, in Fig. 8, we present the photon energy dependence of the OPNMR signal at 3.0 T for two different orientations

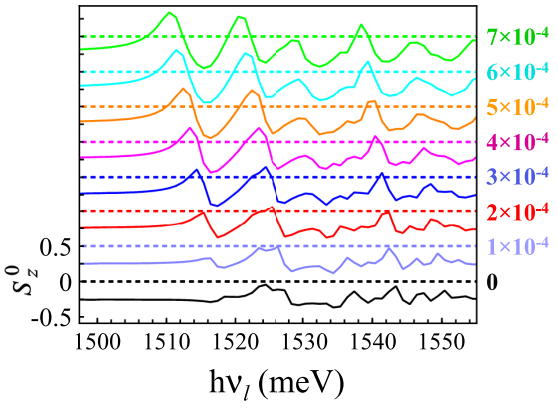

FIG. 6. (Color online) Calculated photon energy dependence of $S_z^0(h\nu_l)$ at 4.9 T for σ^+ light for the values of ε_{zz} given to the right of the plot.

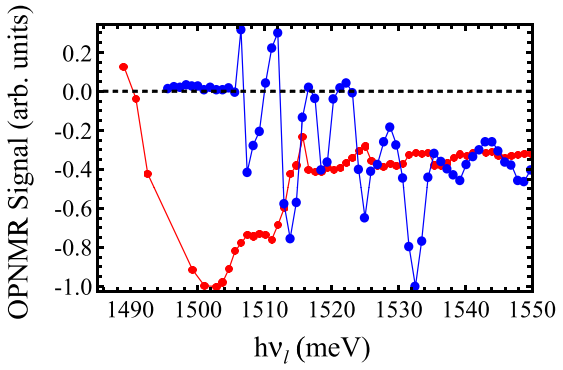

FIG. 7. (Color online) OPNMR photon energy dependence of EA-124 (blue circles) and bulk GaAs (red circles) at 3.0 T using unpolarized light. Data have been normalized to the largest OPNMR signal for each data set.

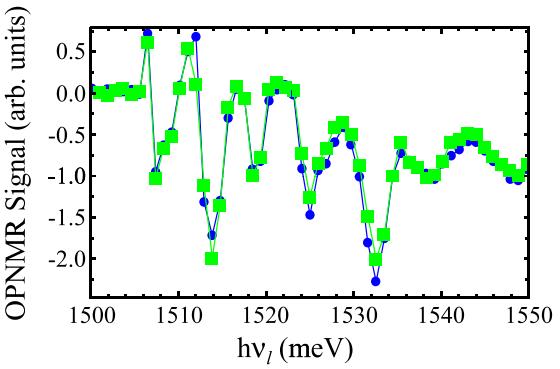

FIG. 8. (Color online) OPNMR photon energy dependence of EA-124 at 3.0 T using unpolarized light oriented at angles of 0° (blue circles) and 6° (green squares) with respect to the magnetic field. Angles refer to the orientation of the growth direction with respect to the magnetic field.

of the sample with respect to the magnetic field. The OPNMR profile of EA-124 is shown to be *insensitive* to tilt angle for small tilt angles, indicating that LL filling factor effects do not contribute significantly under the present experimental conditions, presumably because of the high ambient temperature (∼4.2 K).

V. CONCLUSIONS

To summarize, the strain in a MQW was estimated from the quadrupole splitting observed in the OPNMR spectrum and used as an input parameter in calculations of the MQW's band structure at 4.9 and 9.4 T. From the band structure, photon energy–dependent absorption coefficients for the spin-up and spin-down states of the *CB* were calculated, yielding the electron spin polarization. Using the spin-dependent absorption coefficients, two different quantities were calculated and compared to the experimental OPNMR photon energy dependence. A shift of the energy scale had to be included in the calculations to account for excitonic effects. We find that for an n-doped QW, Eq. (4) provides a reasonable match to the OPNMR data. Deviations could be due to one or more of the following: penetration depth effects, where the optical intensity is not homogeneous across the QW array, nonlinear dependence of the OPNMR signal on absorption at some photon energies, energy-dependent spin relaxation, which has been assumed to be unimportant under our experimental conditions, and effects of sample heating (such as reduction of T_{1s} and/or τ_e). Further work is obviously necessary to reach a quantitative match between theory and experiment.

With the aid of theory, we are able to assign specific features in the OPNMR photon energy dependence to specific transitions in the band structure. Comparison of data acquired from EA-124 to that of bulk GaAs shows that the OPNMR photon energy dependence is strongly influenced not only by quantum confinement effects, but also by strain. Experiments in a tilted field suggest that at these temperatures, the data are insensitive to filling factor effects. Finally, we find that the strained QW exhibits a *HH*/*LH* splitting of ∼4 meV. This separates the *LH* bands from the *HH* bands and, as a result, can substantially change the *CB* spin polarization and hence the nuclear polarization. Calculations show this splitting can be used to increase the maximum possible optically induced electron spin polarization. Application of strain to remove degeneracies in the band structure could be crucial in potential applications such as in spintronics or in quantum computation, which demand initialization of a pure state.

ACKNOWLEDGMENTS

This work was supported by the National Science Foundation (NSF) through Grant No. DMR-1105437. A portion of this work was performed at the National High Magnetic Field Laboratory, which is supported by National Science Foundation Cooperative Agreement No. DMR-1157490, the State of Florida, and the U.S. Department of Energy. This work was performed, in part, at Sandia National Laboratories, a multiprogram laboratory managed and operated by Sandia Corporation, a wholly owned subsidiary of Lockheed Martin Corporation, for the U.S. Department of Energy's National Nuclear Security Administration under Contract No. DE-AC04–94AL85000.

APPENDIX

At sufficiently high magnetic field, the frequencies of the single quantum transitions $m \rightarrow m-1$ of a quadrupolar nucleus are given by

$$\Delta\nu_{m\rightarrow m-1} - \nu_0 = \frac{3(2m-1)eQ}{8I(2I-1)h} V_{ZZ}(3\cos^2\theta - 1) \quad \text{(A1)}$$

where ν_0 is the nuclear Larmor frequency, Q is the quadrupole moment of the nucleus, h is Planck's constant, V_{ZZ} is the component of the EFG along the z axis in the principal axis frame of reference, and θ is the angle between the z axis of the principal axis frame and the magnetic field. For $I = 3/2$, the three single quantum transition frequencies, to first order, are

$$\Delta\nu_{+3/2\rightarrow+1/2} - \nu_0 = \frac{eQ}{4h} V_{ZZ}(3\cos^2\theta - 1) \quad \text{(A2)}$$

$$\Delta\nu_{+1/2\rightarrow-1/2} - \nu_0 = 0 \quad \text{(A3)}$$

$$\Delta\nu_{-1/2\rightarrow-3/2} - \nu_0 = -\frac{eQ}{4h} V_{ZZ}(3\cos^2\theta - 1). \quad \text{(A4)}$$

The quadrupole splitting $\Delta\nu_Q$ is defined as

$$\begin{aligned}\Delta\nu_Q &= \Delta\nu_{+3/2\rightarrow+1/2} - \Delta\nu_{+1/2\rightarrow-1/2} \\ &= \Delta\nu_{+1/2\rightarrow-1/2} - \Delta\nu_{-1/2\rightarrow-3/2}. \quad \text{(A5)}\end{aligned}$$

Hence, we can infer the component of the EFG from the measured quadrupole splitting:

$$V_{ZZ} = \frac{4h}{eQ}\Delta\nu_Q(3\cos^2\theta - 1)^{-1}. \quad \text{(A6)}$$

The differential thermal contraction between the Si substrate and the GaAs films is assumed to produce a biaxial tensile strain. In this case, the z-principal axis of the EFG tensor will be parallel to both the growth direction and the applied magnetic field (i.e., perpendicular to the samples). Hence, the field gradient tensor elements in the principal axis system, V_{IJ}, are equivalent to those of the lab frame, V_{ij}, and $\theta = 0$, so Eq.

(A6) reduces to:

$$V_{ZZ} = \frac{2h}{eQ}\Delta\nu_Q. \tag{A7}$$

The elements V_{ij} are related to the elastic strains, ε_{ij}, by the gradient-elastic tensor S'_{ijkl} [50],

$$V_{IJ} = V_{ij} = \sum_{k,l} S'_{ijkl}\varepsilon_{kl}. \tag{A8}$$

Neglecting ε_{kl} for $k \neq l$ strains, this reduces to

$$\begin{bmatrix} V_{xx} \\ V_{yy} \\ V_{zz} \end{bmatrix} = \begin{bmatrix} S'_{11} & S'_{12} & S'_{12} \\ S'_{12} & S'_{11} & S'_{12} \\ S'_{12} & S'_{12} & S'_{11} \end{bmatrix} \begin{bmatrix} \varepsilon_{xx} \\ \varepsilon_{yy} \\ \varepsilon_{zz} \end{bmatrix} \tag{A9}$$

where we have used $S'_{11} = S'_{22} = S'_{33}$ and $S'_{12} = S'_{13} = S'_{23} = S'_{21} = S'_{31} = S'_{32}$ for GaAs [50]. From Eq. (A9),

$$V_{ZZ} = V_{zz} = S'_{12}\varepsilon_{xx} + S'_{12}\varepsilon_{yy} + S'_{11}\varepsilon_{zz}. \tag{A10}$$

We note that the stresses, and therefore the strains, are equal along the x-and y axes, giving:

$$V_{ZZ} = V_{zz} = 2S'_{12}\varepsilon_{xx} + S'_{11}\varepsilon_{zz} = -S'_{11}\varepsilon_{xx} + S'_{11}\varepsilon_{zz}. \tag{A11}$$

We have used the fact that $2S'_{12} = -S'_{11}$ [50]. The strains along the x and z axes can be related using the compliance tensor S_{ij}. For an isotropic material where $\varepsilon_{kl} = 0$ for $k \neq l$,

$$\begin{bmatrix} \varepsilon_{xx} \\ \varepsilon_{yy} \\ \varepsilon_{zz} \end{bmatrix} = \begin{bmatrix} S_{11} & S_{12} & S_{12} \\ S_{12} & S_{11} & S_{12} \\ S_{12} & S_{12} & S_{11} \end{bmatrix} \begin{bmatrix} \sigma_{xx} \\ \sigma_{yy} \\ \sigma_{zz} \end{bmatrix}. \tag{A12}$$

In the case of equal stress σ along the x and y axes (and no stress along the z axis), the strains are related to the stress by

$$\varepsilon_{xx} = \varepsilon_{yy} = S_{11}\sigma + S_{12}\sigma \tag{A13}$$

TABLE V. Values used to calculate ε_{zz} from the Ga-71 and Ga-69 nuclear quadrupole splitting for EA-124.

Parameter	Value	Units	Reference
S_{11}	1.17	10^{-12} cm^2 dyn^{-1}	[51]
S_{12}	−0.37	10^{-12} cm^2 dyn^{-1}	[51]
S'_{11}	−9.1	10^{15} statC cm^{-3}	[52]
		Ga-71	
Q	1.07	10^{-25} cm^2	[53]
$\Delta\nu_Q$	56	10^3 Hz	
ε_{zz}	−7.7	10^{-4}	
		Ga-69	
Q	1.99	10^{-25} cm^2	[53]
$\Delta\nu_Q$	90	10^3 Hz	
ε_{zz}	−6.6	10^{-4}	

and

$$\varepsilon_{zz} = 2S_{12}\sigma. \tag{A14}$$

From Eqs. (A13) and (A14),

$$\sigma = \frac{\varepsilon_{xx}}{S_{11}+S_{12}} = \frac{\varepsilon_{zz}}{2S_{12}}. \tag{A15}$$

This gives the following relation between ε_{xx} and ε_{zz}

$$\varepsilon_{xx} = \frac{S_{11}+S_{12}}{2S_{12}}\varepsilon_{zz}. \tag{A16}$$

Finally, substituting Eqs. (A11) and (A16) into Eq. (A7) and rearranging:

$$\varepsilon_{zz} = \frac{2h}{eQ}\left(1 - \frac{S_{11}+S_{12}}{2S_{12}}\right)^{-1}\frac{1}{S'_{11}}\Delta\nu_Q. \tag{A17}$$

Numerical values for the constants, quadrupole splitting, and calculated strain using Eq. (A17) are given in Table V.

[1] C. Gmachl, F. Capasso, D. L. Sivco, and A. Y. Cho, Rep. Prog. Phys. **64**, 1533 (2001).
[2] T. Chakraborty and V. M. Apalkov, Adv. Phys. **52**, 455 (2003).
[3] B. S. Williams, Nat. Photon. **1**, 517 (2007).
[4] A. Wade, G. Fedorov, D. Smirnov, S. Kumar, B. S. Williams, Q. Hu, and J. L. Reno, Nat. Photon. **3**, 41 (2009).
[5] G. Scalari, S. Blaser, J. Faist, H. Beere, E. Linfield, D. Ritchie, and G. Davies, Phys. Rev. Lett. **93**, 237403 (2004).
[6] G. Scalari, C. Walther, L. Sirigu, M. L. Sadowski, H. Beere, D. Ritchie, N. Hoyler, M. Giovannini, and J. Faist, Phys. Rev. B **76**, 115305 (2007).
[7] D. Smirnov, C. Becker, O. Drachenko, V. V. Rylkov, H. Page, J. Leotin, and C. Sirtori, Phys. Rev. B. **66**, 121305(R) (2002).
[8] Y. Sun, S. Thompson, and T. Nishida, J. Appl. Phys. **101**, 104503 (2007).
[9] H. Morkoc, B. Sverdlov, and G. B. Gao, Proc. IEEE **81**, 493 (1993).
[10] G. D. Sanders, Y. Sun, F. V. Kyrychenko, C. J. Stanton, G. A. Khodaparast, M. A. Zudov, J. Kono, Y. H. Matsuda, N. Miura, and H. Munekata, Phys. Rev. B **68**, 165205 (2003).
[11] S. E. Barrett, R. Tycko, L. N. Pfeiffer, and K. W. West, Phys. Rev. Lett. **72**, 1368 (1994).
[12] S. E. Hayes, S. Mui, and K. Ramaswamy, J. Chem. Phys. **128**, 052203 (2008).
[13] J. A. Reimer, Solid State Nucl. Magn. Reson. **37**, 3 (2010).
[14] F. Meier and B. Zakharchenya, *Optical Orientation* (Elsevier, Amsterdam, 1984).
[15] S. A. Vitkalov, C. R. Bowers, J. A. Simmons, and J. L. Reno, Phys. Rev. B **61**, 5447 (2000).
[16] P. L. Kuhns, A. Kleinhammes, T. Schmiedel, W. G. Moulton, P. Chabrier, S. Sloan, E. Hughes, and C. R. Bowers, Phys. Rev. B **55**, 7824 (1997).

[17] C. R. Bowers, Solid State Nucl. Magn. Reson. **11**, 11 (1998).
[18] K. Akiba, T. Yuge, S. Kanasugi, K. Nagase, and Y. Hirayama, Phys. Rev. B **87**, 235309 (2013).
[19] S. Mui, K. Ramaswamy, C. J. Stanton, S. A. Crooker, and S. E. Hayes, Phys. Chem. Chem. Phys. **11**, 7031 (2009).
[20] K. Ramaswamy, S. Mui, S. A. Crooker, X. Pan, G. D. Sanders, C. J. Stanton, and S. E. Hayes, Phys. Rev. B **82** 085209 (2010).
[21] M. B. Santos, M. Edirisooriya, T. D. Mishima, C. K. Gaspe, J. Coker, R. E. Doezema, X. Pan, G. D. Sanders, C. J. Stanton, L. C. Tung, and Y-J. Wang, Phys. Procedia **3**, 1201 (2010).
[22] A. Abragam, *Principles of Nuclear Magnetism* (Oxford University Press, Oxford, 1961).
[23] D. Paget, Phys. Rev. B **25**, 4444 (1982).
[24] A. Patel, O. Pasquet, J. Bharatam, E. Hughes, and C. R. Bowers, Phys. Rev. B **60**, R5105(R) (1999).
[25] R. Tycko, S. E. Barrett, G. Dabbagh, L. N. Pfeiffer, and K. W. West, Science **268**, 1460 (1995).
[26] S. E. Barrett, G. Dabbagh, L. N. Pfeiffer, K. W. West, and R. Tycko, Phys. Rev. Lett. **74**, 5112 (1995).
[27] M. I. D'yakonov and V. I. Perel, Zh. Eksp. Teor. Fiz. **60**, 1954 (1971) [Sov. Phys. JETP **33**, 1053 (1971)].
[28] M. I. D'yakonov and V. I. Perel', Fiz. Tverd. Tela (Leningrad) **13**, 3581 (1971) [Sov. Phys. Solid State **13**, 3023 (1972)].
[29] R. J. Elliott, Phys. Rev. **96**, 266 (1954).
[30] Y. Yafet, Solid State Phys. **14**, 1 (1963).
[31] G. L. Bir, A. G. Aronov, and G. E. Pikus, Zh. Eksp. Teor. Fiz. **69**, 1382 (1975) [Sov. Phys. JETP **42**, 705 (1975)].
[32] H. Okamura, D. Heiman, M. Sundaram, and A. C. Gossard, Phys. Rev. B **58**, R15985(R) (1998).
[33] R. G. Shulman and B. J. Wyluda, Phys. Rev. **103**, 1127 (1956).
[34] M. V. Weckwerth, J. A. Simmons, N. E. Harff, M. E. Sherwin, M. A. Blount, W. E. Baca, and H. C. Chui, Superlattices Microstruct. **20**, 561 (1996).
[35] X. Pan, Y. Sun, D. Saha, G. D. Sanders, M. B. Santos, R. E. Doezema, S. E. Hayes, G. Khodaparast, H. Munekata, Y. H. Matsuda, J. Kono, and C. J. Stanton, Proc. SPIE 8461, Spintronics V, pp. 84611P (2012).
[36] W. Gempel, X. Pan, T. Kasturiarachchi, G. D. Sanders, M. Edirisooriya, T. D. Mishima, R. E. Doezema, C. J. Stanton, and M. B. Santos, in *Narrow Gap Semiconductors 2007*, edited by B. Murdin and S. Clowes (Springer, Netherlands, 2008), pp. 213.
[37] G. A. Khodaparast, Y. H. Matsuda, D. Saha, G. D. Sanders, C. J. Stanton, H. Saito, S. Takeyama, T. R. Merritt, C. Feeser, B. W. Wessels, X. Liu, and J. Furdyna, Phys. Rev. B **88**, 235204 (2013).
[38] G. E. Pikus and G. L. Bir, Fiz. Tverd. Tela Leningrad **1**, 1642 (1959) [Sov. Phys. Solid State **1**, 1502 (1960)].
[39] G. L. Bir and G. E. Pikus, *Symmetry and Strain-Induced Effects in Semiconductors* (Wiley, New York, 1974).
[40] Calvin Yi-Ping Chao and S. L. Chuang, Phys. Rev. B **46**, 4110 (1992).
[41] I. Vurgaftman, J. Meyer, and L. Ram-Mohan, J. Appl. Phys. **89**, 5815 (2001).
[42] V. L. Berkovits and V. I. Safarov, Fiz. Tverd. Tela (Leningrad) **20**, 2536 (1978) [Sov. Phys. Solid State **20**, 1468 (1978)].
[43] C. Degen, M. Tomaselli, B. H. Meier, M. M. A. J. Voncken, and A. P. M. Kentgens, Phys. Rev. B **69**, 193303 (2004).
[44] C. M. N. Mateo, A. T. Garcia, F. R. M. Ramos, K. I. Manibog, and A. A. Salvador, J. Appl. Phys. **101**, 073519 (2007).
[45] H. Asai and K. Oe, J. Appl. Phys. **54**, 2052 (1983).
[46] F. H. Pollak and M. Cardona, Phys. Rev. **172**, 816 (1968).
[47] R. I. Cottam and G. A. Saunders, J. Phys. C: Solid State Phys. **6**, 2105 (1973).
[48] W. Stolz, F. E. G. Guimaraes, and K. Ploog, J. Appl. Phys. **63**, 492 (1988).
[49] R. J. Elliott and R. Loudon, J. Phys. Chem. Sol. **15**, 196 (1960).
[50] E. F. Taylor and N. Bloembergen, Phys. Rev. **113**, 431 (1959).
[51] S. Adachi, J. Appl. Phys. **58**, R1 (1985).
[52] R. K. Sundfors, Phys. Rev. B **10**, 4244 (1974).
[53] P. Pyykko, Mol. Phys. **99**, 1617 (2001).